BNL-203519-2018-JAAM

Tunnel-structured Na0.66[Mn0.66Ti0.34]O2-xFx (x < 0.1) cathode for high performance sodium-ion batteries

Q. C. Wang, X. Q. Yang

To be published in "Energy Storage Materials"

May 2018

Chemistry Department

Brookhaven National Laboratory

U.S. Department of Energy

USDOE Office of Energy Efficiency and Renewable Energy (EERE), Vehicle Technologies Office (EE-3V)

DISCLAIMER

Tunnel-structured $Na_{0.66}[Mn_{0.66}Ti_{0.34}]O_{2-x}F_x$ ($x < 0.1$) cathode for high performance sodium-ion batteries

Qin-Chao Wang[1], Qi-Qi Qiu[1], Na Xiao[1], Zheng-Wen Fu[2], Xiao-Jing Wu[2], Xiao-Qing Yang[3], Yong-Ning Zhou[1]*

1. *Department of Materials Science, Fudan University, Shanghai, 200433, P. R. China*
2. *Shanghai Key Laboratory of Molecular Catalysts and Innovative Materials, Department of Chemistry & Laser Chemistry Institute, Fudan University, Shanghai, 200433, P. R. China*
3. *Chemistry Division, Brookhaven National Laboratory, Upton, New York 11973. USA*

* Corresponding author. E-mail: ynzhou@fudan.edu.cn

Abstract:

Sodium-ion batteries (SIBs) are attracting significant research attentions for large-scale energy storage applications. Cathode material is the vital part of SIBs to determine the capacity and cycle performance. Here, a series of F-doped $Na_{0.66}[Mn_{0.66}Ti_{0.34}]O_{2-x}F_x$ ($x < 0.1$) cathodes with tunnel structure are designed and synthesized aiming to enlarge the sodium diffusion paths. The lattice parameters of unit cell are tuned successfully by adjusting F doping amount. $Na_{0.66}[Mn_{0.66}Ti_{0.34}]O_{1.94}F_{0.06}$ with the optimized stoichiometry exhibits a reversible capacity of 97 mAh g^{-1} and promising cycle performance (85 mAh g^{-1} is maintained at 2C after 1000 cycles) with extremely low voltage polarization. More significantly, $Na_{0.66}[Mn_{0.66}Ti_{0.34}]O_{1.94}F_{0.06}$ exhibits superior low temperature performance, owing to the much enhanced thermodynamics and kinetics benefited from F doping. This strategy may open new opportunities to design advanced intercalation-type cathode materials for sodium ion batteries, especially for low-temperature applications.

Keywords: sodium batteries; cathode material; tunnel structure; anion doping; X-ray absorption spectroscopy.

1. Introduction

Sodium-ion batteries (SIBs) attract great attentions for large-scale energy storage applications due to the earth abundance of sodium resources and potential low cost. However, commercialization of SIBs faces the major challenge to find suitable cathode materials. Over the past years, various of cathode materials for SIBs have been designed and studied by imitating the structure and chemistry of cathode materials that function well for Li-ion batteries, including layered oxides,[1-4] tunnel-structured oxides,[5-7] polyanion compounds,[8,9] and organic compounds.[10,11] However, this mimicking strategy is not sufficient for the commercial Na-ion batteries.[12] Specifically, layered $NaTMO_2$ (TM = transition metal) always shows low columbic efficiency during the initial several cycles, compared with no capacity decay after first charge for their Li equivalents, $LiTMO_2$. [1-4, 12-14]

Tunnel-structured compound $Na_{0.44}MnO_2$ with orthorhombic symmetry is a promising cathode material for SIBs, in which Na ions shutters though the large 'S'-shape tunnels reversibility [5]. Mumme et al. first reported the tunnel-structured compound,[5,15] which consisted of double and triple rutile-type chains formed by edge-sharing Mn-O_6 octahedra as well as single chains of corner-sharing MnO_5. Na ions locate in the two type of tunnels in the structure: one is a small tunnel which is fully occupied by Na ions, the other is a large S-shape tunnel which is half filled by Na ions. Only the Na ions located in S-shape tunnel can shutter through the structure reversibly during charge and discharge.[6,16,17] Previous studies confirmed that transition metal substitution in the tunnel-structured $Na_{0.44}MnO_2$ was considered an effective way to improve its Na storage property. Hu et al. had reported that Ti substituted tunnel-structured $Na_{0.44}MnO_2$ had exhibited superior cyclability for aqueous and nonaqueous sodium-ion batteries.[6] The reaction and phase transition pathway can be tuned by Ti substitution. The $Na_{0.66}[Mn_{0.66}Ti_{0.34}]O_2|NaTi_2(PO_4)_3/C$ aqueous sodium-ion full cell exhibits a reversible capacity of 76 mAh g^{-1} with an average operating voltage of 1.2 V at a

current rate of 2C.[5] Air-stable $Na_{0.61}[Mn_{0.27}Fe_{0.34}Ti_{0.39}]O_2$ shows a usable capacity of 90 mAh g^{-1}, registering the highest value among the tunnel-type oxides with an average voltage of 3.56 V, corresponding to Fe^{3+}/Fe^{4+} redox couple.[7] However, Unlike the facile transition metal substitution in layer-structured Na_xTMO_2, it should be very cautious to choose the substitution transition metals for tunnel-structured cathodes in order to still keep the tunnel-type framework.

Anion doping has been considered an effective strategy to improve the electrochemical performance of cathode materials for Li and Na batteries. In the Na_xTMO_2 compounds, O atoms reside in the middle of the transition metals pairs function importantly as bridging atom and forming the TM-O-TM interaction. Anion dopants often effect certain properties by some distance-dependent features at low doping concentration.[18] Density functional theory (DFT) revealed that F doping in cathode materials is positive to elevate the redox potential, improve ionic conductivity and impair TM migration, but negative to cation mixing, such as Li/Ni mixing in high Ni layered cathode materials for lithium batteries.[18] However, for $NaTMO_2$, the cation mixing between TM and Na rarely happens due to the much larger ion radius of Na than TM ions. The F-doping O3-type $NaNi_{1/3}Fe_{1/3}Mn_{1/3}O_2$ can significantly improve the rate performance and capacity retention because of the changing of the binding energy of oxygen.[19]

Here, we tried to tune the lattice parameters of tunnel-structured $Na_{0.66}[Mn_{0.66}Ti_{0.34}]O_2$ cathode material by F doping to construct larger tunnels for facilitating Na transportation. F ions with smaller ionic radius and more negative electronegativity than O ions were intentionally chose in order to import electron hole in O framework and suppress the size of TMO_6 and TMO_5 polyhedrons, leading to enlarged S-shape tunnels. We revealed that the electrochemical performance of $Na_{0.66}[Mn_{0.66}Ti_{0.34}]O_2$ after F doping is remarkably improved, especially at the low temperature. F doping could be an effective strategy for optimizing the cathode materials for SIBs.

2. Experimental section

2.1 Material Synthesis:

A series of F doped tunnel-structured $Na_{0.66}[Mn_{0.66}Ti_{0.34}]O_{2-x}F_x$ (x=0.02, 0.04, 0.06, 0.08) were synthesized by a simple solid-state reaction method using Na_2CO_3, Mn_2O_3, TiO_2 and NaF as precursors in stoichiometric proportion with an excess of 5 mol % Na_2CO_3. After ball-milled in ethanol, the mixture was dry overnight in an oven. The homogenous precursors were calcined at 900 ºC for 20 h in the O_2 atmosphere.

2.2 Material Characterization:

The crystal structure of the synthesized materials were characterized by power X-ray diffraction (XRD). The XRD patterns were collected on an X-ray diffractometer (Bruker D8 Advance, Germeany) with Cu-Ka radiation (λ = 0.1540 nm) at 40 kV, 40 mA from 10° to 80°. XRD refinement was conducted by the Rietveld method using the GSAS+EXPGUI suite.[20-23] The morphology of the synthesis materials were characterized by field emission scanning electron microscopy (FESEM, Cambridge S-360). X-ray absorption spectroscopy (XAS) was performed at beamline 12BM of the Advanced Photon Source (APS) at Argonne National Laboratory and beamline BL14W1 of the Shanghai Synchrotron Radiation Facility (SSRF). Ti and Mn K-edge XAS spectra were collected in transmission mode. The XAS data were processed using Athena and Artemis software packages.[24]

2.3 Electrochemistry:

Working electrodes were prepared by spreading the slurry (70 wt% the active materials, 20 wt% carbon black, 10 wt% polyvinylidenefluoride (PVDF, Sigma-Aldrich) and appropriate amount of N-methyl-2-pyrrolidone (NMP)) onto aluminum foil. The electrodes were dried at 70 ºC under vacuum for 12 h. The active material loading of the working electrode is 2.0 mg cm^{-2}. Coin cells (CR2032) were assembled in an argon-filled glove box. Pure Na foil was used as counter electrode and a glass fiber (GB-100R, ADVANTEC Co., Japan) as separator. The electrolyte was 1 M $NaClO_4$ in a nonaqueous solution of ethylene carbonate/diethyl carbonate

(EC: DEC, 1:1 in volume). Galvanostatic charge-discharge measurements were carried out on a Land CT2001A battery test system (Wuhan, China) with voltage range from 1.5 V to 3.8 V. The current densities and capacities of electrodes were calculated based on the weight of the active materials. Cyclic Voltammetry (CV) and electrochemical impedance spectroscopy (EIS) test were performed on an electrochemical workstation (SP-300, Bio-Logic). CV tests were performed in the voltage range of 1.5 V - 3.8 V vs. Na^+/Na at the scan rates from 0.1 to 1.0 mV s^{-1}. EIS were measured with a voltage amplitude of 5 mV and a frequency range of 10 mHz to 10 MHz.

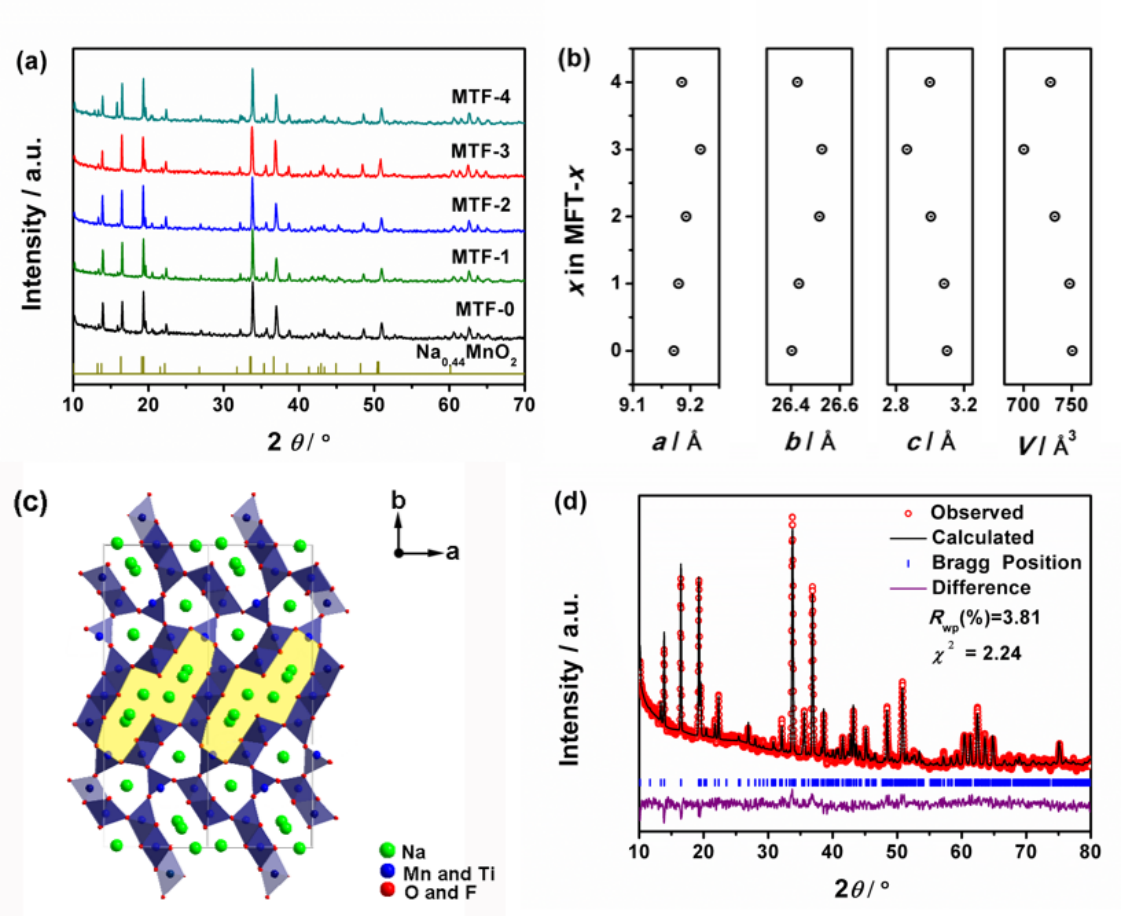

Fig. 1. a) XRD patterns of as-synthesized MTF-*x* (*x* = 0, 1, 2, 3, 4). b) Lattice parameters *a*, *b*, *c* and unit cell volume *V* of MTF-*x*. c) Schematic of the tunnel-structured MTF on the *a*-*b* plane. d) Rietveld refinement patterns of XRD data for MTF-3.

3. Results and Discussion

3.1 Crystal structure

A series of air stable F-doped $Na_{0.66}[Mn_{0.66}Ti_{0.34}]O_{2-x}F_x$ (x=0.02, 0.04, 0.06, 0.08, denoted as MTF-0, MTF-1, MTF-2, MTF-3 and MTF-4, respectively) were synthesized by solid-state reaction method. **Fig. 1a** shows the XRD patterns of these as-synthesized materials. The diffraction peaks of MTF-0 were indexed to a typical tunnel-type structure with a space group of Pbam. Wang et al. had reported that a small amount of P2 phase impurity was produced, when the Mn/Ti ratio was too low or Na/(Mn+Ti) ratio was too high. [5.6] The pure tunnel-type structure of $Na_{0.66}Mn_{0.66}Ti_{0.34}O_2$ can only be obtained at a narrow composition range. With the increasing of F-doping amount, the main structure can be well maintained, while some peaks shift is observed, suggesting that the doped F ions enter O sites in the orthorhombic structure, forming MTF-x solid-solution phase. **Fig. 1b** shows the lattice parameter and volume changes of unit cell derived from XRD. With the increase of F doping up to x = 0.06, the lattice parameter c (the distance between a-b planes) decreases, suggesting the MO_6 and MO_5 polyhedrons are shrinking. However, lattice parameter a and b increase, attributed to the strong electronegativity of F ions, resulting in the expansion of S-type channels. However, when the amount of F doping increase to x = 0.08 (MTF-4), a P2-type layered phase appears, indicating the tunnel structure cannot be stabilized under high F doping amount. In addition, the lattice parameters of MTF-4 start to change in the reversed directions. A schematic of tunnel structure is shown in **Fig. 1c**, the size of S-shape channel is enlarged by the increase of lattice parameter a and b with F doping. Thus, the thermodynamical characteristics for Na storage may become better, facilitating Na intercalation and deintercalation. It is known that Na ions transfer from one unit cell to another along c direction in the S-shape channels. Therefore, the kinetics of Na intercalation/deintercalation can be enhanced by the decreased lattice parameter c, which shortens the Na migration paths from one unit cell to another. From the data above, it is confirmed that F doping can effectively expand a-b plane and decrease lattice parameter c of

the tunnel structure. We believe that the thermodynamics and kinetics for Na storage in tunnel structure could be enhanced by F doping, especially for MTF-3. It is evidenced by the electrochemical performance results shown in **Fig. S1**. The Rietveld refinement of the XRD pattern of MTF-3 is shown in **Fig. 1d**, the lattice parameters of MTF-3 are *a*=9.21774 Å, *b*=26.5267 Å, and *c*=2.86392 Å. Compared with tunnel-type $Na_{0.66}[Mn_{0.66}Ti_{0.34}]O_2$ reported by Hu et al.[5], lattice parameter *a* and *b* are higher while *c* is lower than the reported values of $Na_{0.66}[Mn_{0.66}Ti_{0.34}]O_2$, further confirming the effect of F doping. Scanning electron microscopy (SEM) image (**Fig. S2**) shows that the synthesized MTF-3 mainly consists of rod-like particles in micrometer scale (1-5 μm). EDX mapping indicates all the elements in MTF-3 are distributed homogeneously in the particles.

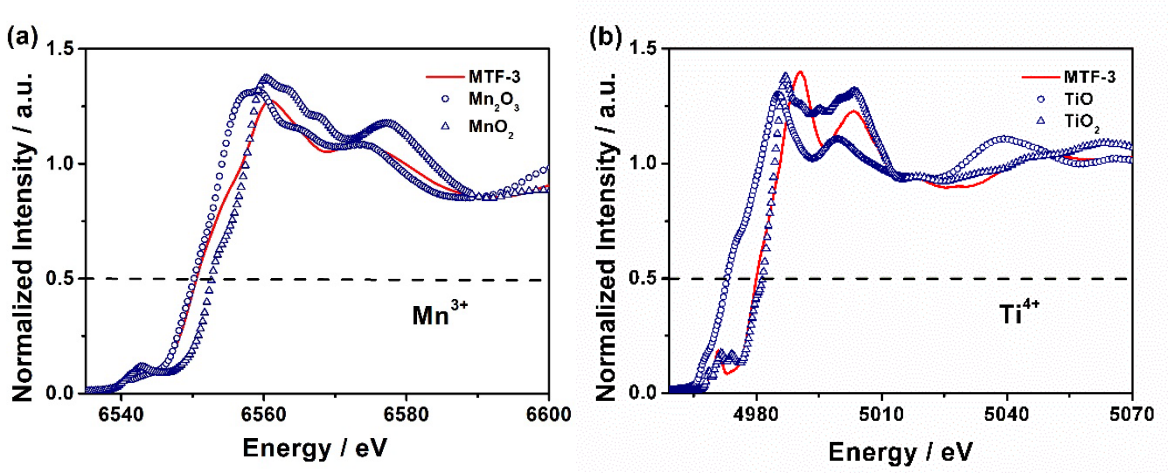

Fig. 2. XANES spectra of a) Mn and b) Ti K-edges of MTF-3 and corresponding metal oxide references with standard valence states, including Mn_2O_3 (Mn^{3+}), MnO_2 (Mn^{2+}), TiO (Ti^{2+}), TiO_2 (Ti^{4+}).

Fig. 2 illustrates the X-ray absorption near edge structure (XANES) spectra of Mn and Ti K-edge for MTF-3. Compared with the standard references (Mn_2O_3, MnO_2, TiO, TiO_2), the valence states of Mn and Ti in the as-synthesized MTF-3 are estimated to be 3+ and 4+, respectively.[24] They are same as the valence states of Mn and Ti in the reported MTF-0,[13,14] implying that F doping does not affect the valence states of transition metals in the tunnel structure.

3.2 Electrochemical performance

The sodium storage performance of MTF-3 were investigated by galvanostatic charge/discharge in the voltage range of 1.5-3.8 V at a current rate of 0.2 C (22 mA g^{-1}), as shown in **Fig. 3a**. The open circuit voltage (OCV) is about 2.75 V (vs. Na^+/Na). The charge-discharge profiles show a typical sloping feature without clear plateaus, which are similar as the undoped MTF-0. The initial charge capacity of MTF-3 is found to be 57 mAh g^{-1}, corresponding to about 0.21 Na extracted per MTF-3. During discharge, a capacity of 96 mAh g^{-1} can be achieved (0.35 Na per MTF-3). It is higher than the discharge capacity of MTF-0 (**Fig. S1**), implying F doping could improve the sodium intercalation property of MTF. After 50 cycles, a reversible capacity of 95 mAh g^{-1} can still be maintained, illustrating good capacity retention. **Fig. 3b** shows the rate capability of MTF-3 electrodes at various rates from 2 C to 20 C. The reversible capacities decrease from 95 mAh g^{-1} to 65 mAh g^{-1} when the current increases from 2 C to 20 C. After the current returns to 2 C, the capacity can recover to 86 mAh g^{-1}, illustrating good rate capability. In addition, the discharge capacity keeps nearly constant after 200 cycles at the current of 2 C. A specific capacity of 85 mAh g^{-1} can be kept even after 1000 cycles at 2 C rate, further confirms the superior long term cycle stability, benefit from the enlarged tunnel structure. Compared with the rate capability and cycle performance of MTF-0 **(Fig. S3)**, these results evidenced that F doping can effectively improve the rate performance and cycle stability of MTF.

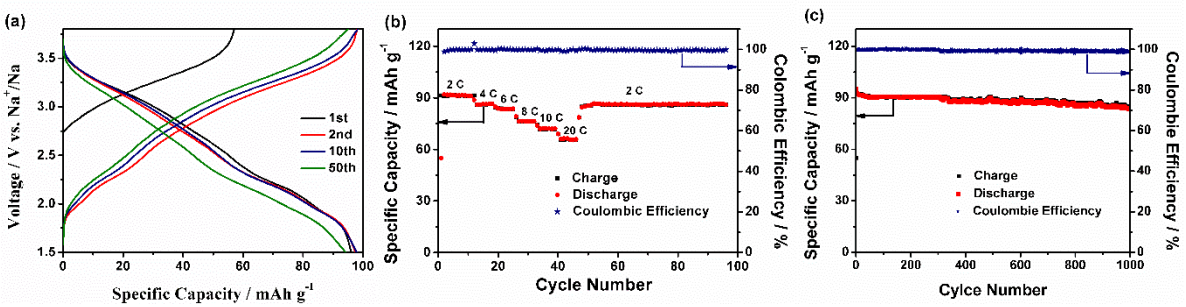

Fig. 3. a) Galvanostatic charge/discharge curves of MTF-3 in the initial 50th cycles at a current rate of 0.2 C (22 mA g^{-1}) in the potential range of 1.5-3.8 V versus Na^+/Na at 25℃. b) Rate capability at various current rates from 2C to 20 C at 25℃. c) The long-cycling performance at 2 C for 1000 cycles at 25℃.

The CV curves of MTF-3 in the first five cycles are presented in **Fig. 4a**. Three pairs of oxidation/reduction peaks locate at 3.30/3.25, 2.27/2.20 and 1.96/1.90 V (vs. Na^+/Na), respectively. These redox peaks are quite symmetric without current decreasing. As shown in **Table S1**, the voltage polarizations between charge and discharge are less than 100 mV, indicating excellent kinetics characteristics and reversibility for MTF-3. For comparison, the redox peaks of MTF-0 shown in **Fig. S4** exhibit much higher voltage polarization than MTF-3, also evidenced by **Table S1**. In addition, the peak voltage difference of MTF-3 between the charge and discharge is much smaller than that of MTF-0 especially at high voltage (**Table S1**), suggesting the effect of F doping on enhancing kinetics and reversibility is more significant at high voltage region.

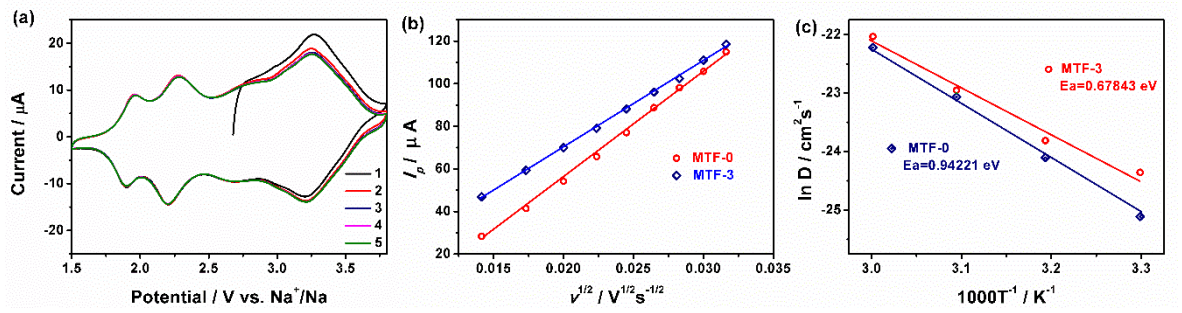

Fig. 4. a) The initial five cyclic voltammograms (CV) of the MTF-3 electrode between 1.5 and 3.8 V versus Na^+/Na at a scan rate of 0.1 mV s^{-1}. b) Plot of the peak current (I_p) as a function of the square root of sweeping rates ($v^{1/2}$) calculated from cyclic voltammograms (CV) at scanning rate from 0.2-1.0 mV s^{-1}. c) ln(D) as a function of inverse temperature obtained from EIS.

3.3 Kinetics characteristics

The ionic diffusion process in MTF are investigated by measuring the CV curves at different scanning rates. The peak shape and peak current evolution of CV curves with sweep rates are

related to the kinetics of Na intercalation/deintercalation in the host structure. **Fig. S5** and **S6** shows CV curves of MTF-0 and MTF-3 at various scan rates from 0.1 to 1.0 mV s^{-1} in the potential range of 1.5-3.8 V. In general, with the increase of scan rates, the peak currents (I_p) of the oxidation and reduction peaks increase. The I_p can be plotted as a function of the scan rate $v^{1/2}$, based on the following equation:[20-23]

$$I_p = 2.69 \times 10^5 n^{3/2} A D^{1/2} v^{1/2} C_0 \quad (1)$$

Where n is the number of electrons per reaction species, A is the area of electrode, D is the diffusion coefficient of Na^+, C_0 is the concentration of Na^+ in the lattice. As shown in **Fig. 4b**, the peak currents I_p shows a good linear dependence on the square root of the scan rate for intercalation process, indicating a diffusion-controlled behavior.[25] The diffusion coefficients (D) for MTF-0 and MTF-3 calculated from Equation (1) are 1.72×10^{-11} and 2.42×10^{-11} cm^2 s^{-1}, respectively.

To further investigate the thermodynamics and kinetics characteristics of F doping in the tunnel structure, electrochemical impedance spectroscopy (EIS) of MTF-0 and MTF-3 was measured. **Fig. S7** shows the measured and fitted EIS results testing from 30 to 60 ℃. By using the equivalent circuit model[26], the fitted results (Z_cal) are well accord with the measured results (Z_msd). The diffusion coefficient (D) and activation energy (E_a) can be calculated by the following equations:[21,23]

$$D = \frac{R^2 T^2 Y_0^2}{n^4 F^4 A^2 C^2} \quad (2)$$

$$\ln D = -\frac{E_a}{k}\frac{1}{T} + lnD_0 \quad (3)$$

Where R is ideal gas constant, T is absolute temperature (K), n is electron transfer number, F is Faraday constant, A is the area of electrode, C is the concentration of Na^+ in the lattice. Y_0 is calculated semi-infinite Warburg diffusion impedance (Z_w).[27] Where, k is Boltzmann constant, E_a is activation energy. The diffusion coefficients of MTF-0 and MTF-3 at 30 ℃ based on Equation (2) are 9.42×10^{-12} and 2.35×10^{-11} cm^2 s^{-1}, which are slightly smaller than

the values derived from CV. The calculated activation energy for MTF-3 based on Equation (3) is 0.678 eV, smaller than 0.942 eV for MTF-0, as shown in **Fig. 4c**. These results manifest that F doping can effectively enhance the thermodynamics and kinetics properties of the tunnel-structured cathode materials.

3.4 Structure evolution

To monitor the structural changes of MTF-3 during Na extraction and insertion, ex situ XRD was conducted at various charge/discharge states in a voltage range of 1.5-3.8 V vs. Na^+/Na. The results are presented in **Fig. 5**. During the charge process, most of diffraction peaks shift continuously to higher angles, indicating the shrinking of the unit cells of MTF-3 upon sodium deintercalation in a solid-solution behavior. At the end of the charge, a new peak can be observed indicating a new phase is formed. However, the new phase cannot be resolved at this stage due to the poor data quality. Compared with the phase transition behavior of $Na_{0.44}Mn_{0.44}Ti_{0.56}O_2$ [6] and $Na_{0.66}Mn_{0.66}Ti_{0.34}O_2$ [5] reported in previous literatures, the peak shift of MTF-3 is much less than $Na_{0.44}Mn_{0.44}Ti_{0.56}O_2$ and $Na_{0.66}Mn_{0.66}Ti_{0.34}O_2$, implying that F doping can effectively prevent the unit cell change of the tunnel structure during desodiation and sodiation, resulting better structure stability.

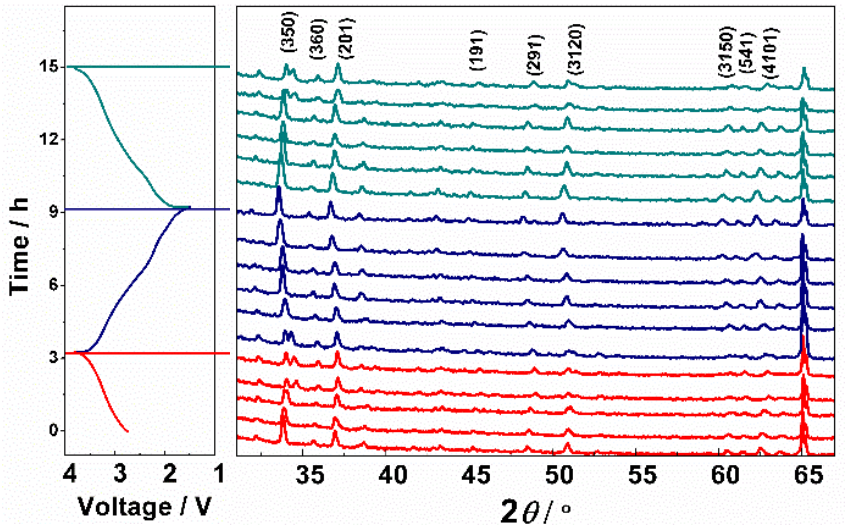

Fig. 5. Ex-situ X-ray diffraction patterns collected during the first charge/discharge and the second charge of Na/MTF-3 cells at a current rate of 0.2 C in the potential range between 1.5 and 3.8 V.

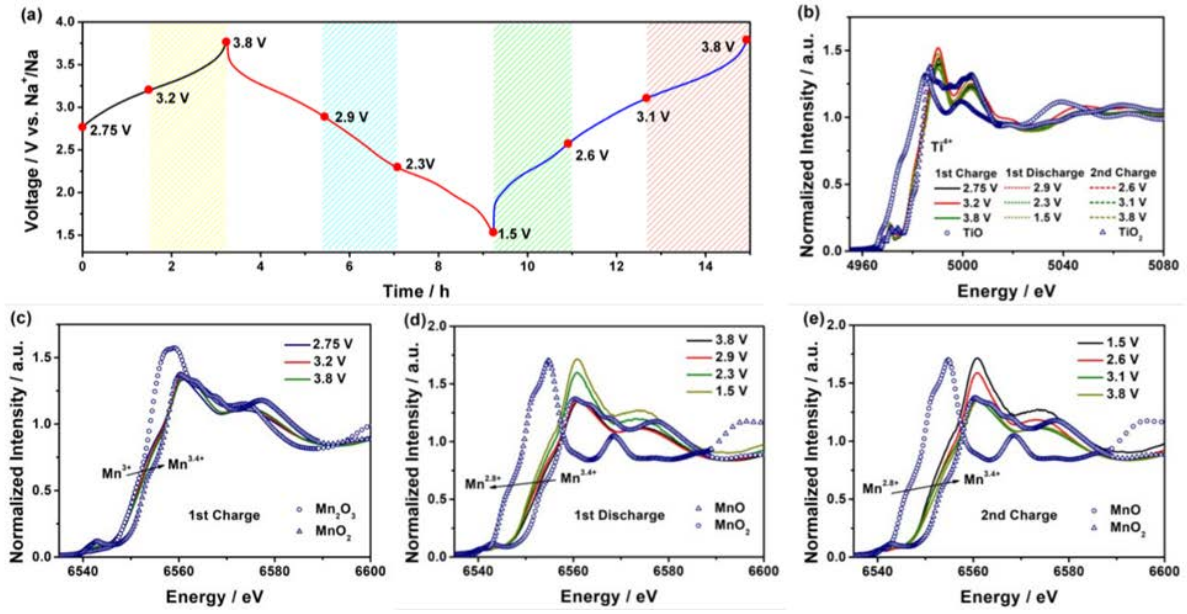

Fig. 6. a) Charge and discharge plots of NCMT-2 electrode for ex XAFS. b), c) and d) Mn K-edge XANES of MTF-3 at various stages during the first charge/discharge and the second charge process, respectively. e) Ti K-edges XANES of MTF-3 at various stages during the first charge/discharge and the second charge processes.

3.5 Charge compensation

The local geometry and valence changes of MTF-3 during the charge/discharge processes are investigated by X-ray absorption spectroscopy (XAS).[28,29] **Fig. 6** shows the X-ray absorption near edge structure (XANES) spectra of Mn and Ti during the first charge, first discharge and second charge processes. The charge/discharge curves and corresponding states where the XAS scans were taken are presented in **Fig. 6a**. indicating very stable Ti^{4+} is maintained with no valence change during sodium intercalation and deintercalation. However, for Mn K-edge spectra in the initial charge and discharge (**Fig. 6c-e**), the white line shifts to higher energy, indicating Mn cation is oxidized to higher valance states ($Mn^{3.0+}$→$Mn^{3.4+}$) during the charge process, corresponding to 0.21 Na^+ deintercalated per MTF-3. It agrees well

with the initial charge capacity of 57 mAh g^{-1}. In the first discharge process (**Fig. 6d**), the XANES spectra of Mn shift back toward lower energy, suggesting the reduction of Mn back to $Mn^{2.8+}$, corresponding to 0.36 Na^+ per MTF-3 intercalated during discharge, agreeing well with the initial discharge capacity of 96 mAh g^{-1}. In the second charge process (**Fig. 6e**), the valance state of Mn undergoes reversed change compared the initial discharge process, suggesting a reversible evolution of the electronic structure and surrounding environment of Mn in MTF-3. The XAS results confirm the charge compensation of MTF-3 during charge and discharge is mainly contributed by Mn.

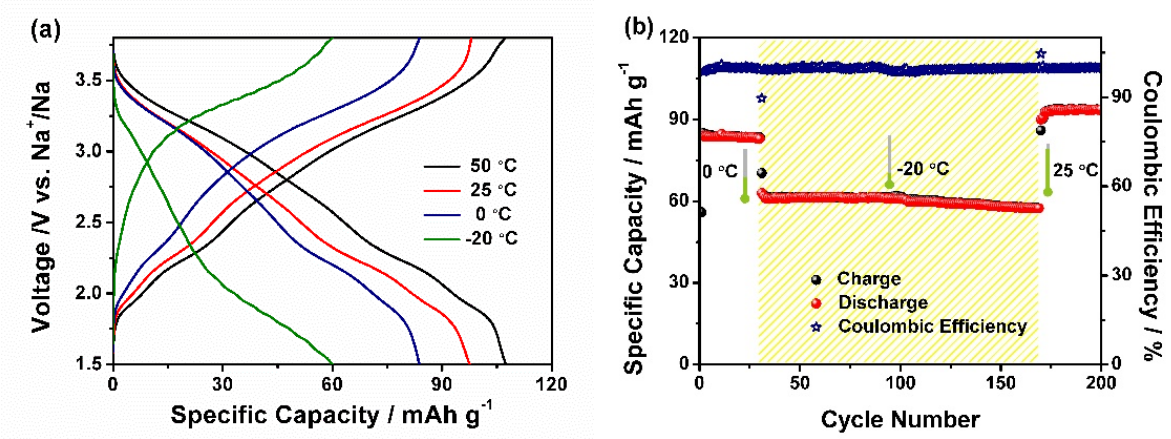

Fig. 7. a) Galvanostatic charge/discharge curves of MTF-3 at a current rate of 0.2 C at 50, 25, 0 and -20 ℃. b) The long-cycling performance of MTF-3 at various temperature of 0 ℃, -20 ℃ and 25 ℃.

3.6 Temperature dependence

From the above results, it is known that F doping results in larger channels for sodium diffusion with better kinetics and thermodynamics, as well as structure stability. Since the low-temperature performance is highly depended on the kinetics and thermodynamics of the electrode materials, the electrochemical performance of MTF-3 and MTF-0 at different temperature were investigated. As shown in the **Fig. 7a**, MTF-3 exhibited a reversible capacity of 107 mAh g^{-1} at 50 ℃, 11 % higher than 96 mAh g^{-1} at room temperature. At 0 ℃, the reversible capacity decreases to 84 mAh g^{-1}, while the voltage polarization is still low.

When the temperature goes down to -20 ℃, a reversible capacity of 60 mAh g^{-1} can still be delivered. For comparison, the discharge capacity of MTF-0 at -20 ℃ is less than 10 mAh g^{-1} as shown in **Fig. S8**. Considering the large ion radius of Na compared with Li, the low temperature could result in very poor kinetics for Na ion transportation in the host framework. The enlarged S-shape tunnels caused by F doping play a key role in facilitate Na transportation at low temperature. On the other hand, the charge-discharge curves of MTF-3 at -20 ºC show increased voltage polarization. It is reported previously that ohmic polarization controlled the overall polarization at room temperature.[30,31] However, at the temperature below -20 ºC, the charge-transfer polarization dominates the overpotential.[31] Thus the increased voltage polarization of MTF-3 at -20 ºC should be mainly contributed by the charge-transfer polarization. The cycle performance of MTF-3 at low temperature is shown in **Fig. 7b**. In the initial 30 cycles, the temperature was set to 0 ºC. A reversible capacity of 84 mAh g^{-1} is maintained with negligible capacity fading. After 30 cycles, the temperature is set down to -20 ºC, a reversible capacity of 61.5 mAh g^{-1} is retained with the average capacity fading of 0.04 % per cycle, exhibiting superior cycle performance at such a low temperature. When the temperature is reset to room temperature (25 ºC), the capacity recovers to 93 mAh g^{-1}, suggesting strong tolerance at various temperatures. It should be noted that the primary particle size of MTF-3 are in the range of 1-5 μm and not optimized. We believe the low-temperature performance can be further improved by optimizing the particle size and surface coating.[32]

4. Conclusion

In this work, a series of F doped tunnel-structured $Na_{0.66}[Mn_{0.66}Ti_{0.34}]O_{2-x}F_x$ (x=0.02, 0.04, 0.06, 0.08) cathode materials are designed and synthesized for SIBs. F doping affects the unit cells with increased *a* and *b* lattice parameters and decreased c lattice parameter, resulting in enlarged S-shape channels for sodium transportation with better kinetics and thermodynamics, as well as structure stability. Among them, MTF-3 delivers the highest reversible capacity of

97 mAh g^{-1} at 0.2 C with excellent capacity retention in 1000 cycles at 2 C current rate. Both CV and EIS measurements confirm that diffusion coefficient can be increased significantly by F doping. In addition, F doping shows marked effectiveness to improve the low temperature performance of MTF at -20 ºC. MTF-3 delivers a stable reversible capacity of 84 mAh g^{-1} at 0 ºC and 61.5 mAh g^{-1} at -20 ºC with superior capacity retention, while MTF-0 only yields a very low capacity of 6-7 mAh g^{-1} at -20 ºC. XRD results prove the single phase evolution character during charge and discharge, and less lattice changes of MTF-3 compared with MTF-0, benefiting for the cycle performance in MTF-3. XAS results reveal that the charge compensation of MTF-3 during cycling is only contributed by Mn-ion redox. This work opens new opportunities to design advanced intercalation-type cathode materials for sodium ion batteries, especially for low temperature applications.

Supporting Information

Galvanostatic discharge curves, rate capability, long-cycling performance, cyclic voltammograms, electrochemical impedance spectroscopy and scanning electronic microscopy image.

Acknowledgement

The work at Fudan University was supported by the NSFC (No.51502039) and 1000 Youth Talents Plan. The work at Brookhaven National Laboratory was supported by the U.S. Department of Energy, the Assistant Secretary for Energy Efficiency and Renewable Energy, Office of Vehicle Technologies through Advanced Battery Material Research (BMR) program under Contract No. DE-SC0012704. The authors thank beamline BL14W1 and BL14B1 of the Shanghai Synchrotron Radiation Facility in China and beamline 12BM of

Advanced Photon Source at Argonne National Laboratory, supported by the U.S. Department of Energy, Basic Energy Science, under Contract No. DE-AC02-06CH11357.

References

[1] N. A. Katcho, J. Carrasco, D. Saurel, E. Gonzalo, M. Han, F. Aguesse, T. Rojo, Origins of bistability and Na ion mobility difference in P2- and O3-$Na_{2/3}Fe_{2/3}Mn_{1/3}O_2$ cathode polymorphs. *Adv. Energy Mater. 7* (2017) 1601477.

[2] D. Kim, S.-H. Kang, M. Slater, S. Rood, J. T. Vaughey, N. Karan, M. Balasubramanian, C. S. Johnson, Enabling sodium batteries using lithium-substituted sodium layered transition metal oxide cathodes, *Adv. Energy Mater. 1* (2011) 333-336.

[3] E. Talaie, V. Duffort, H. L. Smith, B. Fultz, L. F. Nazar, Structure of the high voltage phase of layered P2-$Na_{2/3}[Mn_{1/2}Fe_{1/2}]O_2$ and the positive effect of Ni substitution on its stability, *Energy Environ. Sci. 8* (2015) 2512-2523.

[4] C. Fang, Y. Huang, W. Zhang, J. Han, Z. Deng, Y. Cao, H. Yang, Routes to high energy cathodes of sodium-ion batteries, *Adv. Energy Mater. 6* (2016) 1501727.

[5] Y. Wang, L. Mu, J. Liu, Z. Yang, X. Yu, L. Gu, Y.-S. Hu, H. Li, X.-Q. Yang, L. Chen, X. Huang, A novel high capacity positive electrode material with tunnel-type structure for aqueous sodium-ion batteries, *Adv. Energy Mater. 5* (2015) 1501005.

[6] Y. Wang, J. Liu, B. Lee, R. Qiao, Z. Yang, S. Xu, X. Yu, L. Gu, Y. S. Hu, W. Yang, K. Kang, H. Li, X. Q. Yang, L. Chen, X. Huang, Ti-substituted tunnel-type $Na_{0.44}MnO_2$ oxide as a negative electrode for aqueous sodium-ion batteries, *Nat. Commun. 6* (2015) 6401.

[7] S. Xu, Y. Wang, L. Ben, Y. Lyu, N. Song, Z. Yang, Y. Li, L. Mu, H.-T. Yang, L. Gu, Y.-S. Hu, H. Li, Z.-H. Cheng, L. Chen, X. Huang, Fe-based tunnel-type $Na_{0.61}[Mn_{0.27}Fe_{0.34}Ti_{0.39}]O_2$ designed by a new strategy as a cathode material for sodium-ion batteries, *Adv. Energy Mater.5* (2015) 1501156.

[8] P. Barpanda, G. Oyama, S. Nishimura, S. C. Chung, A. Yamada, A 3.8-V earth-abundant sodium battery electrode, *Nat. Commun.* 5 (2014) 4358.

[9] Z. Jian, W. Han, X. Lu, H. Yang, Y.-S. Hu, J. Zhou, Z. Zhou, J. Li, W. Chen, D. Chen, L. Chen, Superior electrochemical performance and storage mechanism of $Na_3V_2(PO_4)_3$ cathode for room-temperature sodium-ion batteries. *Adv. Energy Mater. 3* (2013) 156-160.

[10] B. Dunn, H. Kamath, J.-M. Tarascon, Electrical energy storage for the grid: a battery of choices, *Science 334* (2011) 928-935.

[11] M. Armand, S. Grugeon, H. Vezin, S. Laruelle, P. Ribiere, P. Poizot, J. M. Tarascon, Conjugated dicarboxylate anodes for Li-ion batteries, *Nat. Mater. 8* (2009) 120-125.

[12] S.-W. Kim, D.-H. Seo, X. Ma, G. Ceder, K. Kang, Electrode materials for rechargeable sodiumion batteries: potential alternatives to current lithium-ion batteries, *Adv. Energy Mater.* 2 (2012) 710-721.

[13] A. R. Armstrong, P. G. Bruce, Synthesis of layered $LiMnO_2$ as an electrode for rechargeable lithium batteries, *Nature* 381 (1996) 499.

[14] Q.-C. Wang, E. Hu, Y. Pan, N. Xiao, F. Hong, Z.-W. Fu, X.-J. Wu, S.-M. Bak, X.-Q. Yang, Y.-N. Zhou, Utilizing Co^{2+}/Co^{3+} redox couple in P2-layered $Na_{0.66}Co_{0.22}Mn_{0.44}Ti_{0.34}O_2$ cathode for sodium-ion batteries, *Adv. Sci.* (2017) 1700219.

[15] W. G. Mumme, The structure of $Na_4Mn_4Ti_5O_{18}$, *Acta Cryst. B24* (1968) 1114-1120.

[16] Y. Cao, L. Xiao, W. Wang, D. Choi, Z. Nie, J. Yu, L. V. Saraf, Z. Yang, J. Liu, Reversible sodium ion insertion in single crystalline manganese oxide nanowires with long cycle life, *Adv. Mater. 23* (2011) 3155-3160.

[17] E. Hosono, T. Saito, J. Hoshino, M. Okubo, Y. Saito, D. Nishio-Hamane, T. Kudo, H. Zhou, High power Na-ion rechargeable battery with single-crystalline $Na_{0.44}MnO_2$ nanowire Electrode, *J. Mater. Chem. A 217* (2012) 43-46.

[18] F. Kong, C. Liang, R. C. Longo, D.-H. Yeon, Y. Zheng, J.-H. Park, S.-G. Doo, K. Cho, Conflicting roles of anion doping on the electrochemical performance of Li-ion battery cathode materials. *Chem. Mater. 28* (2016) 6942-6952.

[19] Q. Zhang, Y. Huang, Y. Liu, S. Sun, K. Wang, Y. Li, X. Li, J. Han, Y. Huang, F-doped O3-$NaNi_{1/3}Fe_{1/3}Mn_{1/3}O_2$ as high-performance cathode materials for sodium-ion batteries, *Sci. China Mater. 60* (2017) 629-636.

[20] J. L. Yue, W. W. Yin, M. H. Cao, S. Zulipiya, Y. N. Zhou, Z. W. Fu, A quinary layer transition metal oxide of $NaNi_{1/4}Co_{1/4}Fe_{1/4}Mn_{1/8}Ti_{1/8}O_2$ as a high-rate-capability and long-cycle-life cathode material for rechargeable sodium ion batteries, *Chem. Commun. 51* (2015) 15712-15715.

[21] K. Tang, X. Yu, J. Sun, H. Li, X. Huang, Kinetic analysis on $LiFePO_4$ thin films by CV, GITT, and EIS, *Electrochim. Acta 56* (2011) 4869-4875.

[22] J. Zheng, Y. Hou, Y. Duan, X. Song, Y. Wei, T. Liu, J. Hu, H. Guo, Z. Zhuo, L. Liu, Z. Chang, X. Wang, D. Zherebetskyy, Y. Fang, Y. Lin, K. Xu, L.-W. Wang, Y. Wu, F. Pan, Janus solid-liquid interface enabling ultrahigh charging and discharging rate for advanced lithium-ion batteries, *Nano Lett. 15* (2015) 6102-6109.

[23] J.-L. Yue, Y.-N. Zhou, X. Yu, S.-M. Bak, X.-Q. Yang, Z.-W. Fu, O3-type layered transition metal oxide $Na(NiCoFeTi)_{1/4}O_2$ as a high rate and long cycle life cathode material for sodium ion batteries, *J. Mater. Chem. A 3* (2015) 23261-23267.

[24] Y.-N. Zhou, J. Ma, E. Hu, X. Yu, L. Gu, K.-W. Nam, L. Chen, Z. Wang, X.-Q. Yang, Tuning charge–discharge induced unit cell breathing in layer-structured cathode materials for lithium-ion batteries, *Nat. Commun.* (2014) 5381.

[25] D. Cao, C. Yin, D. Shi, Z. Fu, J. Zhang, C. Li, Cubic perovskite fluoride as open framework cathode for Na-ion batteries, *Adv. Funct. Mater. 27* (2017) 1701130.

[26] R. Shanmugam, W. Lai, Study of transport properties and interfacial kinetics of $Na_{2/3}[Ni_{1/3}Mn_xTi_{2/3-x}]O_2$ (x = 0, 1/3) as electrodes for Na-ion batteries, *J. Electrochem. Soc. 162* (2014) A8-A14.

[27] X. Fang, F. Lin, D. Nordlund, M. Mecklenburg, M. Ge, J. Rong, A. Zhang, C. Shen, Y. Liu, Y. Cao, M. M. Doeff, C. Zhou, Atomic insights into the enhanced surface stability in high voltage cathode materials by ultrathin coating, *Adv. Funct. Mater. 27* (2017) 1602873.

[28] Y.-N. Zhou, J.-L. Yue, E. Hu, H. Li, L. Gu, K.-W. Nam, S.-M. Bak, X. Yu, J. Liu, J. Bai, E. Dooryhee, Z.-W. Fu, X.-Q. Yang, High-rate charging induced intermediate phases and structural changes of layer-structured cathode for lithium-ion batteries, *Adv. Energy Mater. 6* (2016) 1600597

[29] Y.-N. Zhou, J.-J. Ding, K.-W. Nam, X. Yu, S.-M. Bak, E. Hu, J. Liu, J. Bai, H. Li, Z.-W. Fu, X.-Q. Yang, Phase transition behavior of $NaCrO_2$ during sodium extraction studied by synchrotron-based X-ray diffraction and absorption spectroscopy. *J. Mater. Chem. A 1* (2013) 11130.

[30] H. Liu, F. C. Strobridge, O. J. Borkiewicz, K. M. Wiaderek, K. W. Chapman, P. J. Chupas, C. P. Grey, Capturing metastable structures during high-rate cycling of $LiFePO_4$ nanoparticle electrodes, *Science 344* (2014) 1252817.

[31] Y. You, H. R. Yao, S. Xin, Y. X. Yin, T. T. Zuo, C. P. Yang, Y. G. Guo, Y. Cui, L. J. Wan, J. B. Goodenough, Subzero-temperature cathode for a sodium-ion battery, *Adv. Mater. 28* (2016) 7243-7248.

[32] M. J. Young, H.-D. Schnabel, A. M. Holder, S. M. George, C. B. Musgrave, Band diagram and rate analysis of thin film spinel $LiMn_2O_4$ formed by electrochemical conversion of ALD-grown MnO, *Adv. Funct. Mater. 26* (2016) 7895-7907.

Supporting Information

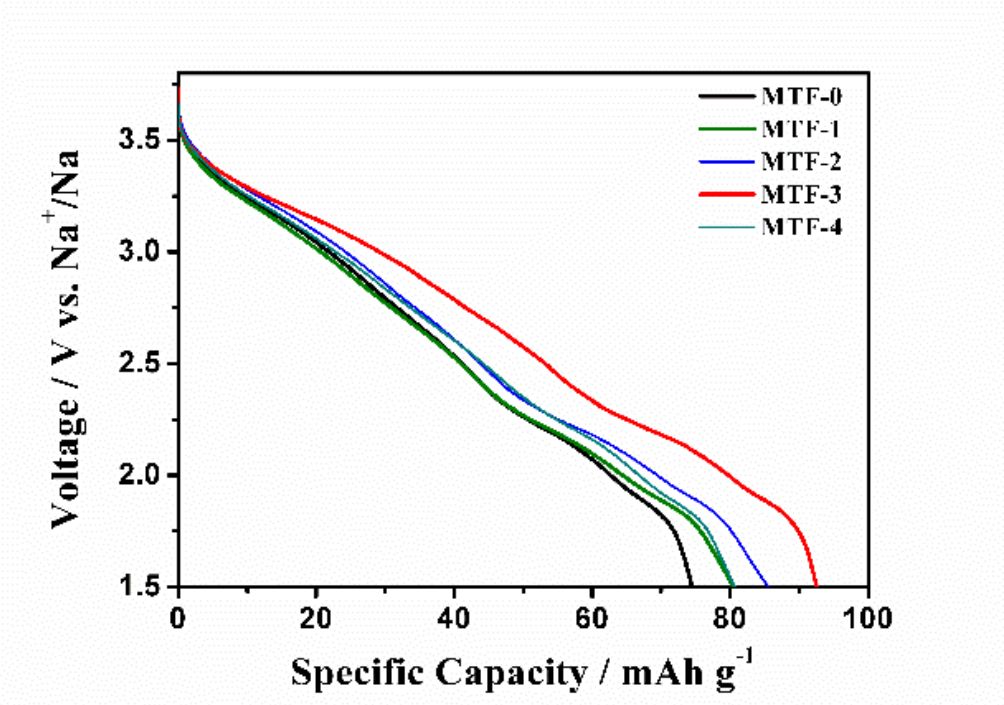

Fig. S1. Galvanostatic discharge curves of MTF-0 (black), MTF-1 (olive), MTF-2 (blue), MTF-3 (red) and MTF-4 (cyan) in the initial cycle at a current rate of 0.2 C (22 mA g^{-1}) in the potential range of 1.5 - 3.8 V versus Na^+/Na.

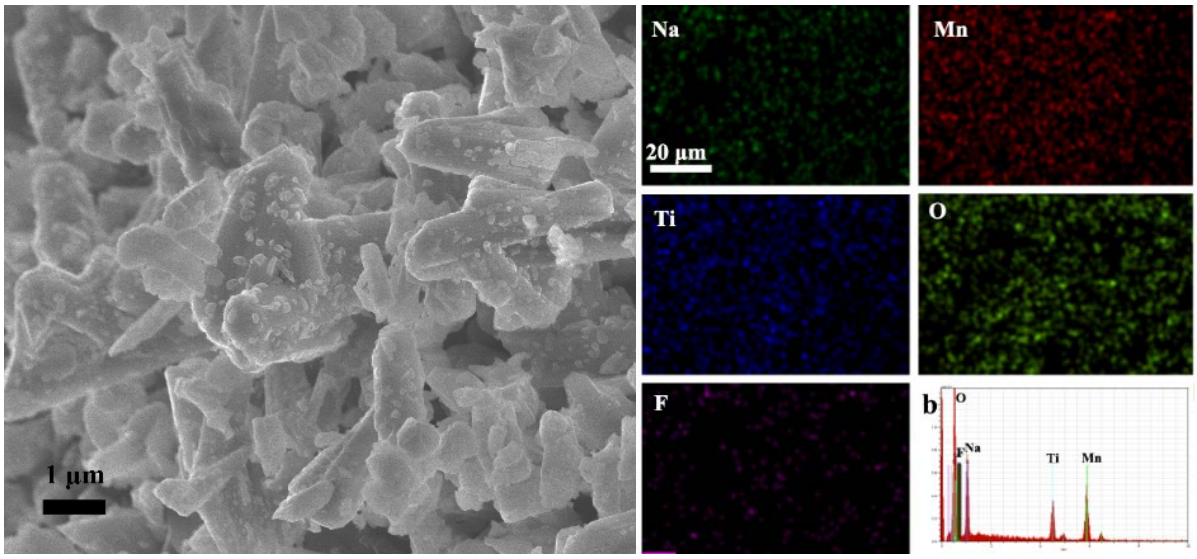

Fig. S2. The SEM image (a) of MTF-3 and corresponding EDX mapping (b) of element Na, Mn, Ti, O and F.

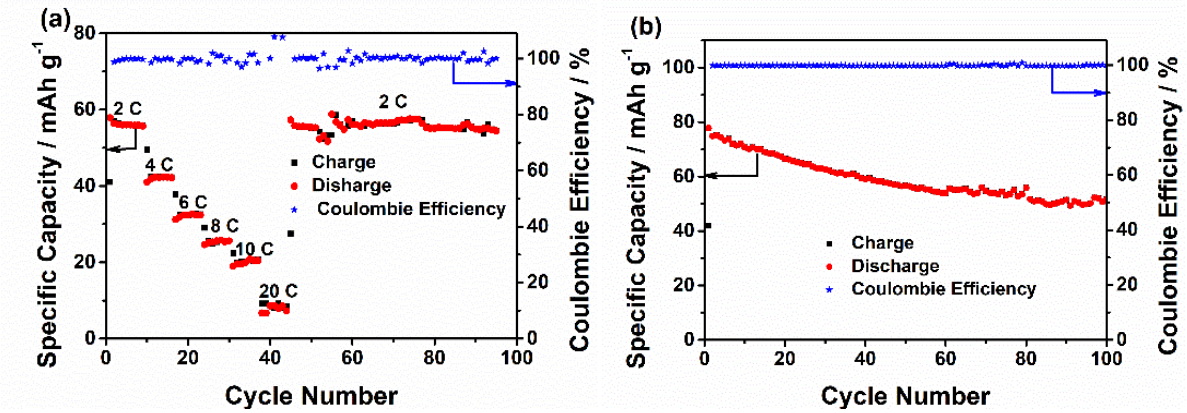

Fig. S3. (a) Rate capability for MTF-0 at various current rates from 2C to 20 C at 25 °C in the potential range of 1.5-3.8 V versus Na^+/Na. (b) The long-cycling performance of MTF-0 at 0.2 C for 100 cycles at 25°C.

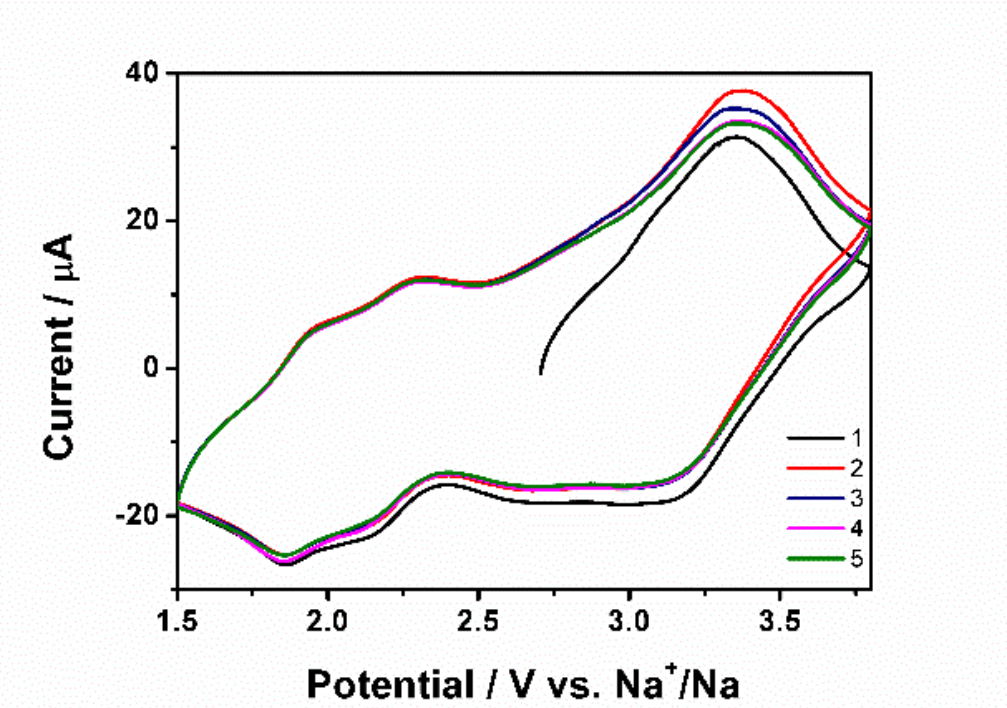

Fig. S4. The initial five cyclic voltammograms (CV) of the MTF-0 electrode between 1.5 and 3.8 V versus Na^+/Na at a scan rate of 0.1 mV s^{-1}.

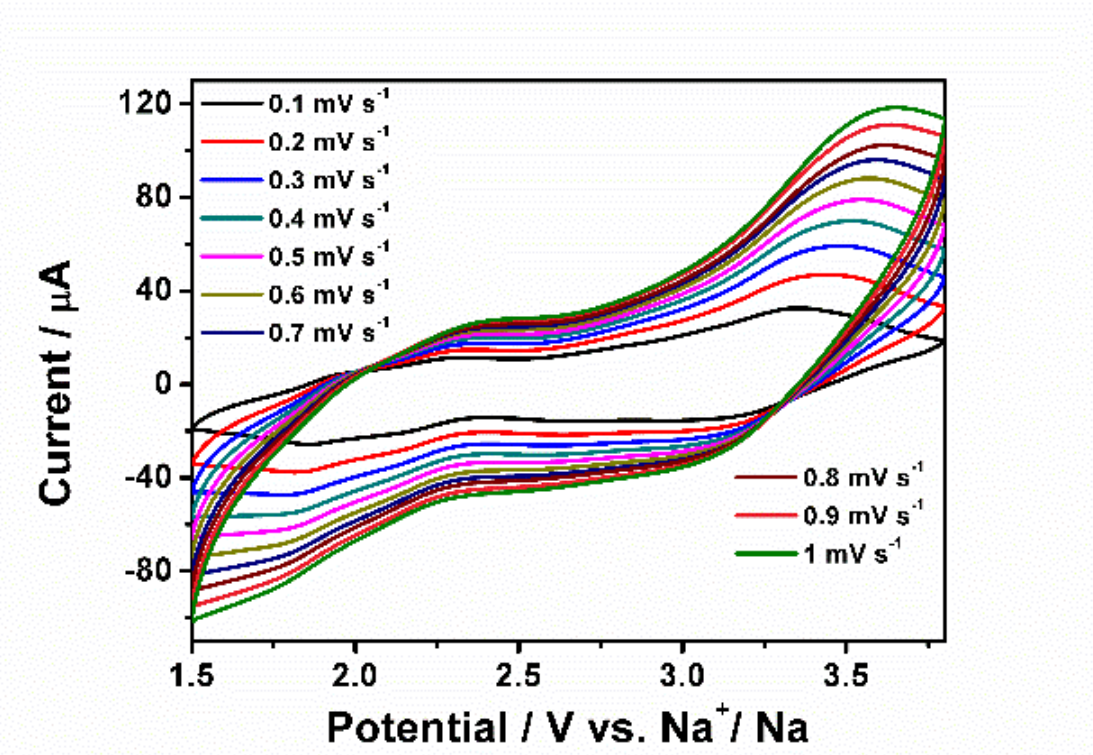

Fig. S5. CV profiles for MTF-0 electrode at various scan rates of 0.1, 0.2, 0.3, 0.4, 0.5, 0.6, 0.7, 0.8, 0.9 and 1 mV s^{-1}.

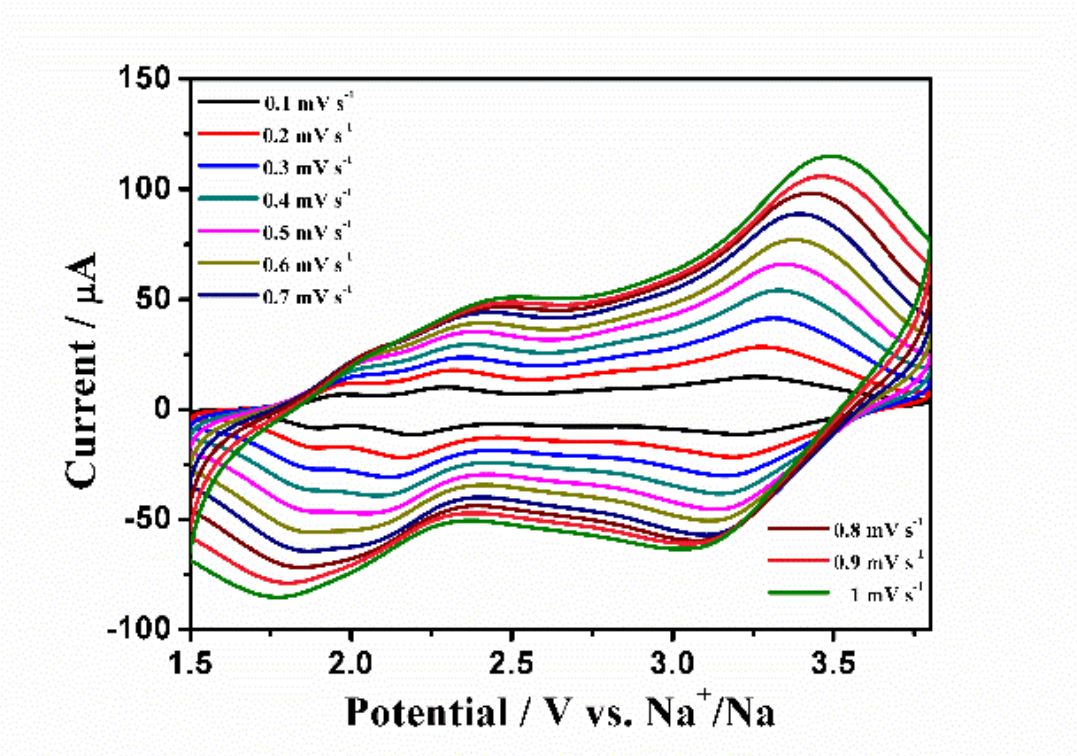

Fig. S6. CV profiles for MTF-3 electrode at various scan rates of 0.1, 0.2, 0.3, 0.4, 0.5, 0.6, 0.7, 0.8, 0.9 and 1 mV s^{-1}.

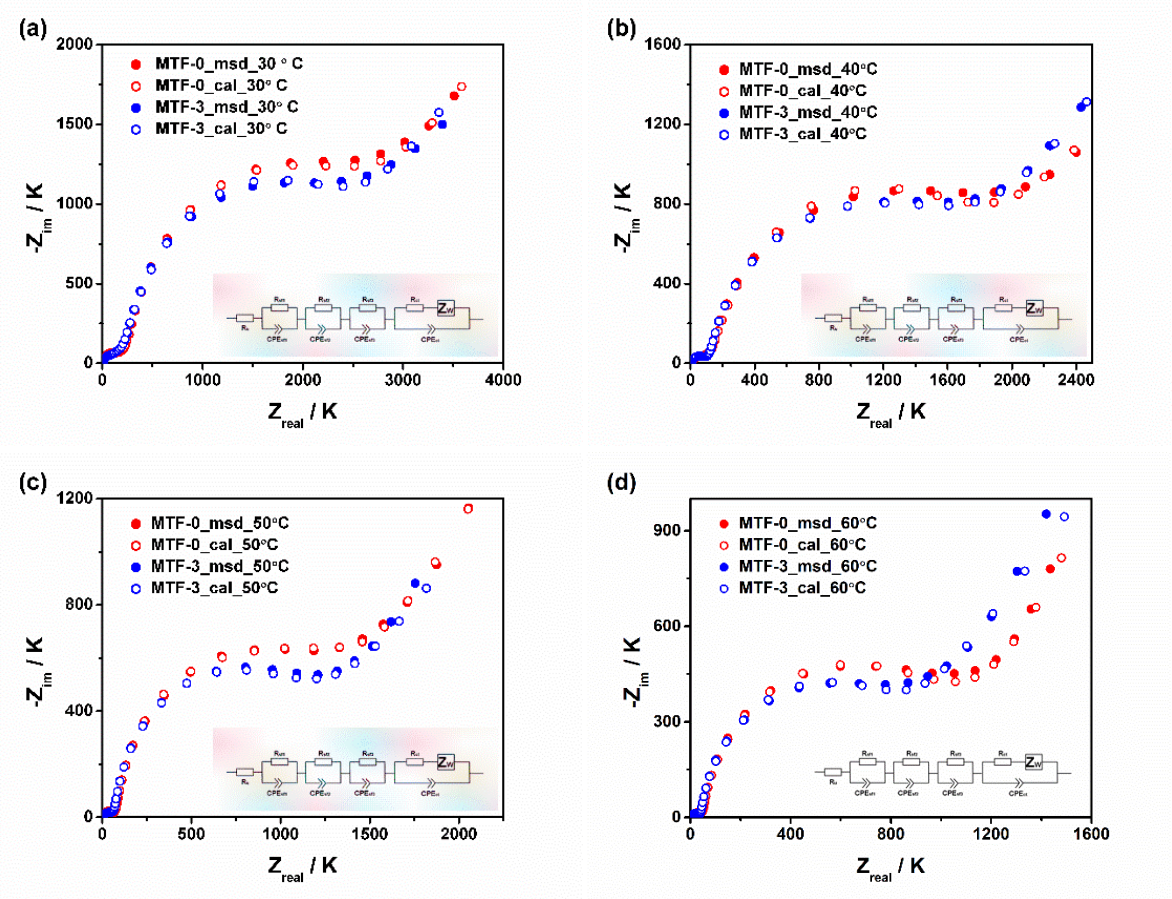

Fig. S7. Nyquist plots of measured electrochemical impedance spectroscopy (EIS) results (Z_msd) and calculated results (Z_cal) from equivalent circuit model of the MTF-0 (red) and MTF-3 (blue) electrode at 30 (a), 40 (b), 50 (c) and 60 ºC (d), inserting images is the equivalent circuit model for nyquist plots.

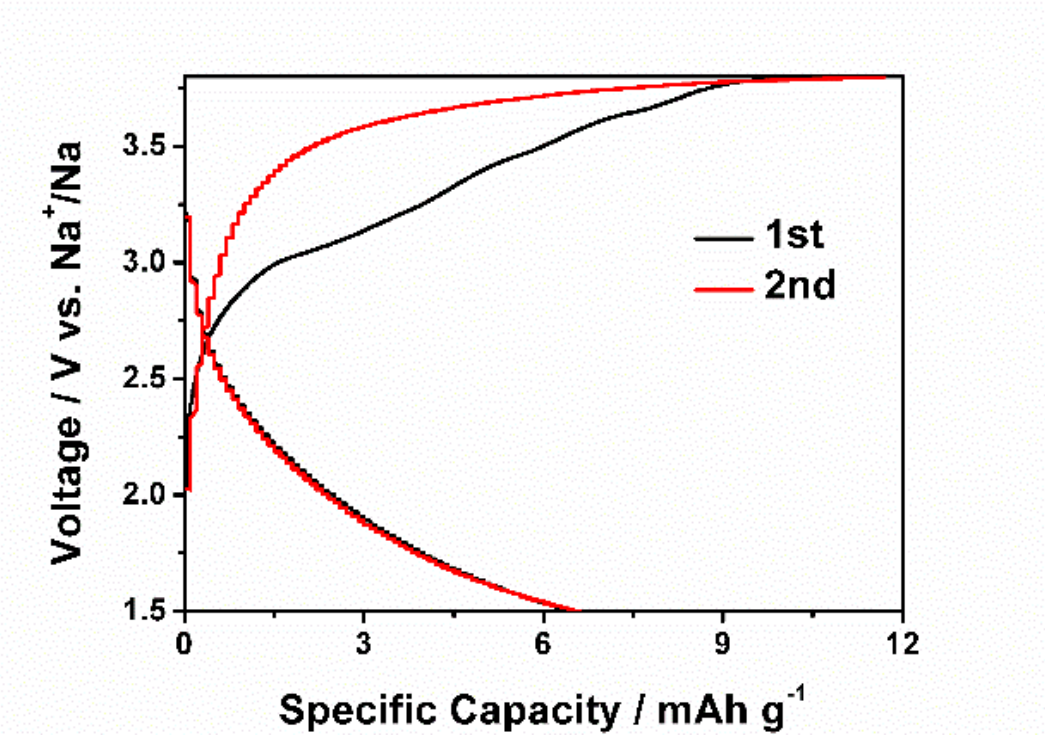

Fig. S8. The galvanostatic charge/discharge curves of MTF-0 for the first (black) and the second (red) cycle at -20 ºC.

Table S1. The peak potential of MTF-0 and MTF-3 in the CV at 0.1 mV s^{-1} for positive and negative scanning. The ∆V is the voltage polarizations between charge (positive scan) and discharge (negative scan).

Sample	Scanning	Potential / V	∆V / V	Potential / V	∆V / V	Potential / V	∆V / V
MTF-0	Positive	1.93	0.08	2.29	0.13	3.35	0.18
	Negative	1.85		2.16		3.17	
MTF-3	Positive	1.96	0.06	2.27	0.07	3.30	0.05
	Negative	1.90		2.20		3.25	